Physica E 48 (2013) 191–197

Contents lists available at SciVerse ScienceDirect

Physica E

journal homepage: www.elsevier.com/locate/physe

Guided modes and quantum Goos–Hänchen shift in graphene waveguide: Influence of a velocity barrier

Y. Wang [a], Y. Liu [b], B. Wang [a,*]

[a] School of Physics and Engineering, Sun Yat-sen University, 510275 Guangzhou, China
[b] School of Engineering, Sun Yat-sen University, 510275 Guangzhou, China

HIGHLIGHTS

- A cutoff velocity determining the appearance of each guided mode occurs.
- The conductance of graphene waveguide presents a quantized feature for velocity.
- Goos–Hänchen shift in graphene waveguide can be controlled by the velocity barrier.

GRAPHICAL ABSTRACT

The graphene waveguide in the presence of a velocity barrier presents a cutoff velocity for each guide mode and velocity-controlled Goos–Hänchen shift.

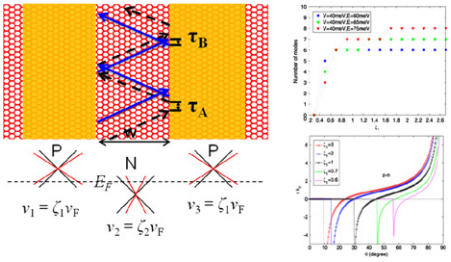

ARTICLE INFO

Article history:
Received 22 October 2012
Received in revised form
2 December 2012
Accepted 9 January 2013
Available online 19 January 2013

ABSTRACT

The influence of velocity on the guided modes, localized current density inside the channel and the Goos–Hänchen shift at the interface of graphene waveguide in the presence of a velocity barrier is investigated theoretically. It is found that each guided mode has a cutoff velocity determining the appearance of the oscillating wave mode and the velocity in the barrier regions can control the number of guided modes and the distribution of localized current density inside the channel. The number of guided modes and the conduction of graphene waveguide along the channel present a quantized feature for velocity. Finally, it is also indicated that the Goos–Hänchen shift at the interface of graphene waveguide can be well controlled by changing the velocity in barrier region.

1. Introduction

Graphene, an atomic layer of crystalline carbon [1], has zero band gaps near the Dirac point and linear dispersion which leads to many novel electronic properties [2,3], and has shown potential application prospect in graphene-based nanoelectronic device [4–6]. Experimentally, P (hole-like) or N (electron-like) regions in graphene can be achieved by using a combination of top/bottom electrostatic gates [7]. Theoretically, the Dirac equation describing propagation for carriers in graphene-based p or n regions shows the similarity of the Helmholtz equation describing electromagnetic wave propagation in optic medium. As a result, electrons or holes in graphene-based medium behave like photons and exhibit analogous wave phenomena. For example, owing to the helicity nature of Dirac fermions [8], electronic negative refractive effect can be created by the interband scattering at the interface of a graphene bipolar p–n junction [9]. The electronic negative refraction based on graphene PN junction is applied to a Veselago lens or electronic prism instead of two-dimensional electron gas (2DEG) systems in conventional semiconductor device. It is also shown that the electron supercollimation can be achieved by an array of periodic graphene PN junction [10], which is called graphene superlattice leading to many unique electronic transport properties [11–13]. In addition, as an analogy of optical

* Corresponding author. Tel.: +86 20 8411 5692; fax: +86 20 8411 3293.
E-mail address: bwang6367@gmail.com (B. Wang).

1386-9477/$ - see front matter © 2013 Elsevier B.V. All rights reserved.
http://dx.doi.org/10.1016/j.physe.2013.01.008

Goos–Hänchen shift, which is referred to a lateral shift between the reflected beam and the incident beam occurring at the interface of two different materials on total internal reflection [14], the quantum Goos–Hänchen effect for Dirac fermions is found at the interfaces of graphene PN junction [15], strained barrier and magnetic barrier [16–18]. A most recent work also shows the giant Goos–Hänchen shift occurs at the interface of graphene double potential barriers [19].

As one of the novel nanoelectronic devices, graphene waveguide has triggered extensive research interest in theory and experiment. Recently, the electron waveguide has been suggested by using graphene in the presence of magnetic field owing to magnetic confinement [20,21], local strain due to the strain-induced confinement [22], multiple segments of armchair-edged nanoribbons due to geometric constraints of the structure [23], and electrostatic potential owing to the confinement of the quantum well [24–28]. The bound states of electron in graphene quantum well have been theoretically investigated by Pereira et al. [24] and Zhang et al. [25]. The guided efficiency and localized current density inside the channel of waveguide were experimentally demonstrated by Williams et al. [28]. Here, we pay attention to the graphene waveguide induced by electric confinement, in the presence of a velocity barrier. On one hand, the gate-controlled guiding of electrons in graphene is experimentally shown with different carriers' densities in different regions, which can lead to a distribution of carriers' velocity. Instead of doped graphene, most recent investigations show that the Fermi velocity of charge carriers is made to vary in space by placing a grounded metal plane close to graphene [29], or by modulating a two-dimensional electron with a long-wavelength periodic potential of honeycomb symmetry [30]. On the other hand, it is demonstrated that the distribution of velocity in graphene has a strong influence on electronic transport through velocity-modulated nanostructures [31–36], such as a velocity barrier in graphene investigated by Raoux et al. [29,31], velocity-modulated graphene superlattices demonstrated by Krstajić and Vasilopoulos [32] and graphene with correlated disorder in velocity profiles shown by Esmailpour et al. [36].

Based on the previous method used to investigate the guided modes and Goos–Hänchen shift [15–17,24,25], in this paper, we will present the influence of velocity on transport properties of graphene waveguide in the presence of a velocity barrier, including the guided modes as main characteristics of waveguide, localized current density inside the channel of waveguide and the Goos–Hänchen shift at the PN interface of waveguide on total internal reflection. The guided modes and Goos–Hänchen shift in graphene quantum well can be controlled by the magnitude of potential well [15,25]. However, in this present work, it is found that a velocity barrier can be also used to manipulate the bound states and the Goos–Hänchen shift of electron in graphene waveguide.

2. Theory

The massless Dirac–Weyl model for the graphene-based medium, where the Fermi velocity v and potential barrier V change as the functions $v=v(\mathbf{r})$ and $V=V(\mathbf{r})$ of the 2D position $\mathbf{r}$, respectively, is well described by [29,35]

$$-i\hbar\sqrt{v(\mathbf{r})}\ \boldsymbol{\sigma}\cdot\nabla_{\mathbf{r}}[\sqrt{v(\mathbf{r})}\boldsymbol{\psi}(\mathbf{r})]+V(\mathbf{r})\boldsymbol{\psi}(\mathbf{r})=E\ \boldsymbol{\psi}(\mathbf{r}), \tag{1}$$

where $\boldsymbol{\sigma}=(\boldsymbol{\sigma}_x, \boldsymbol{\sigma}_y)$ is the Pauli spin matrices, $\boldsymbol{\psi}(\mathbf{r})=[\psi_A(\mathbf{r}), \psi_B(\mathbf{r})]^T$ is the two-component wave function consisting of the smooth enveloping functions $\boldsymbol{\psi}_A(\mathbf{r})$ and $\boldsymbol{\psi}_B(\mathbf{r})$ associated with the A and B sublattices of graphene, and E is the eigenenergy. When using the model, it is assumed that the velocity variation is slow enough on the scale of the lattice constant. Considering the y directional momentum as a constant and the velocity varying only along the x direction as $v=v(x)$ in the velocity-modulated graphene quantum well, as shown in Fig. 1, a auxiliary spinor can be introduced and written in the form as $\Phi(\mathbf{r})=v(\mathbf{r})^{1/2}\ \boldsymbol{\psi}(\mathbf{r})=v(x)^{1/2}\ \boldsymbol{\psi}(x)\ \exp\ (ik_y)$, and then, the Dirac equation can be reduced as

$$-i\hbar v(x)(\partial_x \mp k_y)\Phi_{A(B)}(x)=(E-V(x))\Phi_{B(A)}(x) \tag{2}$$

The confined states are caused by total internal reflection (TIR) at the p–n interfaces. In other words, the guiding of Dirac fermions is localized in the middle well region and the evanescent states exist in left and right barrier regions. Thus, in the quantum well regime, the wave functions of the bound states satisfying Eq. (2) are written as

$$\begin{cases} \Phi_{LA}(x)=\alpha e^{\kappa(x+w/2)}, & (x<-w/2),\\ \Phi_{LB}(x)=i\gamma_1\alpha e^{\kappa(x+w/2)}, & (x<-w/2),\\ \Phi_{MA}(x)=C\sin(k_x x)+D\cos(k_x x), & (-w/2\le x\le w/2),\\ \Phi_{MB}(x)=-i[C\cos(k_x x+\theta)-D\sin(k_x x+\theta)], & (-w/2\le x\le w/2),\\ \Phi_{RA}(x)=\beta e^{-\kappa(x-w/2)}, & (x>w/2),\\ \Phi_{RB}(x)=i\gamma_2\beta e^{-\kappa(x-w/2)}, & (x>w/2), \end{cases} \tag{3}$$

where $\kappa=(k_y^2-k^2)^{1/2}$ with $k=(E-V)/\hbar\zeta_1 v_F$ ($v_F\approx c/300$) owing to the TIR, $k_x=sign(E)(k_F^2/\zeta_2^2-k_y^2)^{1/2}$ with $k_F=E/\hbar v_F$, the incident angle θ satisfies $\theta=arctan(k_y/k_x)$, α and β are the amplitude of the left and right evanescent waves respectively, $\gamma_1=(-\kappa+k_y)/k$ and $\gamma_2=(\kappa+k_y)/k$. This expression $k=(E-V)/\hbar\zeta_1 v_F$ and $k_x=sign(E)(k_F^2/\zeta_2^2-k_y^2)^{1/2}$ have the advantage, which can well describe the propagating states and evanescent states in a unified form [26]. In fact, the definition is consistent with the expression $k=s'|E-V|/\hbar\zeta_1 v_F$ with $s'=sign(E-V)$ [25], owing to $E-V=s'|E-V|$. For $E<V$, the tunneling through potential barrier is called Klein tunneling and clearly demonstrates interband scattering at the p–n junction's interface due to the helicity nature of the Dirac fermions [8]. For $\zeta_2=1$ and $\zeta_1>1$, a velocity well is combined with the graphene quantum well, as shown in Fig. 1, on the other hand, a velocity barrier is applied to the structure for $\zeta_2=1$ and $\zeta_1<1$. Using the continuity of wave functions at the boundaries $x=\pm w/2$, $\Phi_{LA}(-w/2)=\Phi_{MA}(-w/2)$, $\Phi_{LB}(-w/2)=\Phi_{MB}(-w/2)$, $\Phi_{MA}(w/2)=\Phi_{RA}(w/2)$ and $\Phi_{MB}(w/2)=\Phi_{RB}(w/2)$, the coefficient ratio D/C in Eq. (3) can be obtained by

$$\begin{aligned} D/C&=\frac{-\gamma_1\sin(k_x w/2)+\cos(-k_x w/2+\theta)}{-\gamma_1\cos(k_x w/2)+\sin(-k_x w/2+\theta)}\\ &=\frac{\gamma_2\sin(k_x w/2)+\cos(k_x w/2+\theta)}{-\gamma_2\cos(k_x w/2)+\sin(k_x w/2+\theta)}, \end{aligned} \tag{4}$$

Substituting $\gamma_1=(-\kappa+k_y)/k$ and $\gamma_2=(\kappa+k_y)/k$ into Eq. (4), we can further give the bound states' eigenmodes satisfying the following transcendental equation:

$$\begin{aligned} &[\zeta_1\zeta_2 {k_y}^2-E(E-V)]\sin(k_x w)\\ &\quad+\sqrt{E^2-{\zeta_2}^2{k_y}^2}\sqrt{{\zeta_1}^2{k_y}^2-(E-V)^2}\cos(k_x w)=0 \end{aligned} \tag{5}$$

Eq. (5) can be further rewritten as

$$\tan(k_x w)=\sqrt{E^2-{\zeta_2}^2{k_y}^2}\sqrt{{\zeta_1}^2{k_y}^2-(E-V)^2}/[E(E-V)-\zeta_1\zeta_2{k_y}^2] \tag{6}$$

In order to describe the right-hand-side of Eq. (6), we can conveniently define $F(k_x w)$ as a function of $k_x w$ with the following dimensionless form:

$$F(k_x w)=k_x w\sqrt{(k_y w)^2-(kw)^2}/[k_F wkw/\zeta_2-(k_y w)^2]$$

Goos–Hänchen (GH) effect, as an interference effect on total internal reflection, can be explained by the stationary-phase approximation [18,19,37], or the Gaussian beam method

[15–17]. In this present work, the later is used. Owing to the symmetry of the velocity-modulated graphene quantum well, the reflection phases and GH shifts at interfaces $x=\pm w/2$ are the same. Therefore, we can only consider the reflection at the interface $x=w/2$. Using Eq. (2), left and right wave functions at the p–n interface $x=w/2$ can be written as

$$\begin{cases} \Phi_{AL}(x)=e^{ik_x x}+re^{-ik_x x}, & (x\le w/2),\\ \Phi_{BL}(x)=e^{i(k_x x+\theta)}-re^{-i(k_x x+\theta)}, & (x\le w/2),\\ \Phi_{AR}(x)=\beta e^{-\kappa(x-w/2)}, & (x>w/2),\\ \Phi_{BR}(x)=i\gamma_2\beta e^{-\kappa(x-w/2)}, & (x>w/2), \end{cases} \tag{7}$$

where θ is the incident angle and r is the reflection coefficient. The wavevector k_x in the left well region should be real with $E>\hbar\zeta_2 v_F k_y$ if incident energy is positive, and the wavevector in the right barrier's region is imaginary with $(E-V)^2/\hbar^2\zeta_1^2 v_F^2-k_y^2\le 0$, owing to the TIR, therefore, the TIR angle can be defined by

$$\theta_c=\arcsin\left[\zeta_2(E-V)/\zeta_1 E\right] \tag{8}$$

Taking into account the continuity of wave functions at the p–n interface $x=w/2$, we can obtain the reflection coefficient r,

$$r(k_y)=e^{i\varphi_r}=\frac{-i\gamma_2+e^{i\theta}}{i\gamma_2+e^{-i\theta}}e^{ik_x w}, \tag{9}$$

where φ_r is the reflection phase. By using the Eq. (9), the reflection phase can be obtained by

$$\varphi_r=2\delta-k_x w, \tag{10}$$

where δ satisfies $\tan\delta=\tan\theta+ss'\gamma_2\sec\theta$ with $s=\mathrm{sign}(E)$ and $s'=\mathrm{sign}(E-V)$. When a finite-sized incident Gaussian electron beam is considered, the wave function of the incident and reflection beam satisfying Eq. (2) can be assumed to be

$$\Phi_{in}(x,y)=\int_{-\infty}^{\infty}dk_y u(k_y-\bar{k})e^{ik_y y+ik_x(k_y)x}\begin{bmatrix}1\\ e^{i\theta(k_y)}\end{bmatrix}, \tag{11a}$$

$$\Phi_r(x,y)=\int_{-\infty}^{\infty}dk_y r(k_y)u(k_y-\bar{k})e^{ik_y y-ik_x(k_y)x}\begin{bmatrix}1\\ e^{i\theta(k_y)}\end{bmatrix} \tag{11b}$$

In the above wave function, a Gaussian envelope is taken by $u(k_y-\bar{k})=\exp(-(k_y-\bar{k})^2/2\Delta_k^2)$ so that the wavepacket is sharply peaked at $k_y=\bar{k}$ with $\bar{k}\in(0,k_F)$ and the incident angle is given by $\theta(k_y)\in(0,\pi/2)$. The k_y dependent $\theta(k_y)$, $k_x(k_y)$ and $r(k_y)$ are approximately expanded by Taylor series and retained with the first order term, and then the upper GH shifts τ_A, lower GH shifts τ_B and the average shifts $\tau=(\tau_A+\tau_B)/2$ can be obtained by [17]

$$\begin{cases} \tau_A=-\varphi_r'(\bar{k})+2k_x'(\bar{k})x,\\ \tau_B=-\varphi_r'(\bar{k})+2\theta'(\bar{k})+2k_x'(\bar{k})x,\\ \tau=-\varphi_r'(\bar{k})+\theta'(\bar{k})+2k_x'(\bar{k})x. \end{cases} \tag{12}$$

In the above expression, a coordinate-dependent term $2k_x'(\bar{k})x$ and an opposite term $-\varphi_r'(\bar{k})$ make all the GH shifts be independent of the choice of the coordinate of the interface at which total internal reflection will take place. Substituting the reflection phase of Eq. (10) into Eq. (12), the upper, lower and average GH shifts of electron beam at the interfaces of the velocity and potential barrier can be obtained by

$$\begin{cases} \tau_A k_F=-2\frac{\zeta_2\sec^2\phi+ss'\gamma_2 k_F/\kappa+\zeta_2 ss'\gamma_2\sec\theta\tan\theta}{\sec\phi+\gamma_2{}^2\sec\theta+2ss'\gamma_2\tan\theta},\\ \tau_B k_F=2\zeta_2\sec\theta-2\frac{\zeta_2\sec^2\theta+ss'\gamma_2 k_F/\kappa+\zeta_2 ss'\gamma_2\sec\theta\tan\theta}{\sec\theta+\gamma_2{}^2\sec\theta+2ss'\gamma_2\tan\theta},\\ \tau k_F=\zeta_2\sec\theta-2\frac{\zeta_2\sec^2\theta+ss'\gamma_2 k_F/\kappa+\zeta_2 ss'\gamma_2\sec\theta\tan\theta}{\sec\theta+\gamma_2{}^2\sec\theta+2ss'\gamma_2\tan\theta}. \end{cases} \tag{13}$$

3. Results and discussion

3.1. Guided modes

Eq. (6) shows that the dispersion relation of bound states is decided by the combination of potential barrier and velocity barrier. Previous works have presented the influence of potential on guided modes, so we focus on the modulation on guided modes from the velocity barrier. The confinement of electron is caused by the reflection at the interfaces of graphene waveguide, thus, the dispersion relation of bound states can determine the guided modes. To obtain the guided modes, the graphical method is proposed to solve the transcendental Eq. (6). As shown in Fig. 2, the intersections between the solid curves $\tan(k_x w)$and the dashed curves $F(k_x w)$ demonstrate the existence of guided modes. From Fig. 2(a) to Fig. 2(f), it is clearly seen that the number of guided modes first increases with increasing the velocity ζ_1 of barrier regions and then reaches maximum. In addition, the change of modes is quite obvious if ζ_1 is small. As shown in Fig. 2(a)–(c), the numbers of guided modes denoted by the intersections are 2, 3 and 5, respectively. This means that one can adjust the distribution of velocity in graphene waveguide to control the appearance of the higher-order modes. Experimentally, it is convenient to adjust the distribution of velocity by changing the distance between the grounded metal plane and graphene [29].

Fig. 3 further presents the number $M(\zeta_1)$ of guided modes as a function of the velocity ζ_1 in barrier regions at some specific incident energies. In spite of different incident energies, it is clearly shown that the number of guided modes first increases and then maintains a maximum. More importantly, there is a cutoff velocity, which determines the appearance of the fundamental mode. As shown in the inset of Fig. 3, when the number of guided mode is equal to 1, the cutoff velocities of fundamental mode corresponding to the incident energies 60 meV, 65 meV, and 75 meV are 0.34, 0.38 and 0.47, respectively. In other words, the cutoff velocity increases with the increase of the incident energy. In addition, from the inset of Fig. 3, it is also shown that

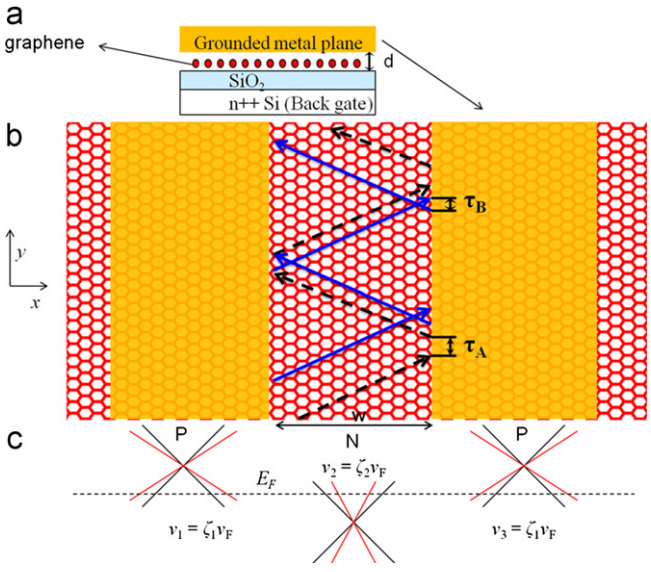

Fig. 1. (a) Cross-section view of barrier regions under the grounded metal plane. (b) Schematic diagram of the graphene waveguide in the presence of a velocity barrier, where the yellow shaded regions denote the barrier regions below the grounded metal plane. (c) The distribution of Fermi velocities in three regions is indicated by the slope of the linear spectrum of quasiparticles in graphene, with the Fermi energy E_F locating in valence bands of barrier regions and conduction bands of well regions.

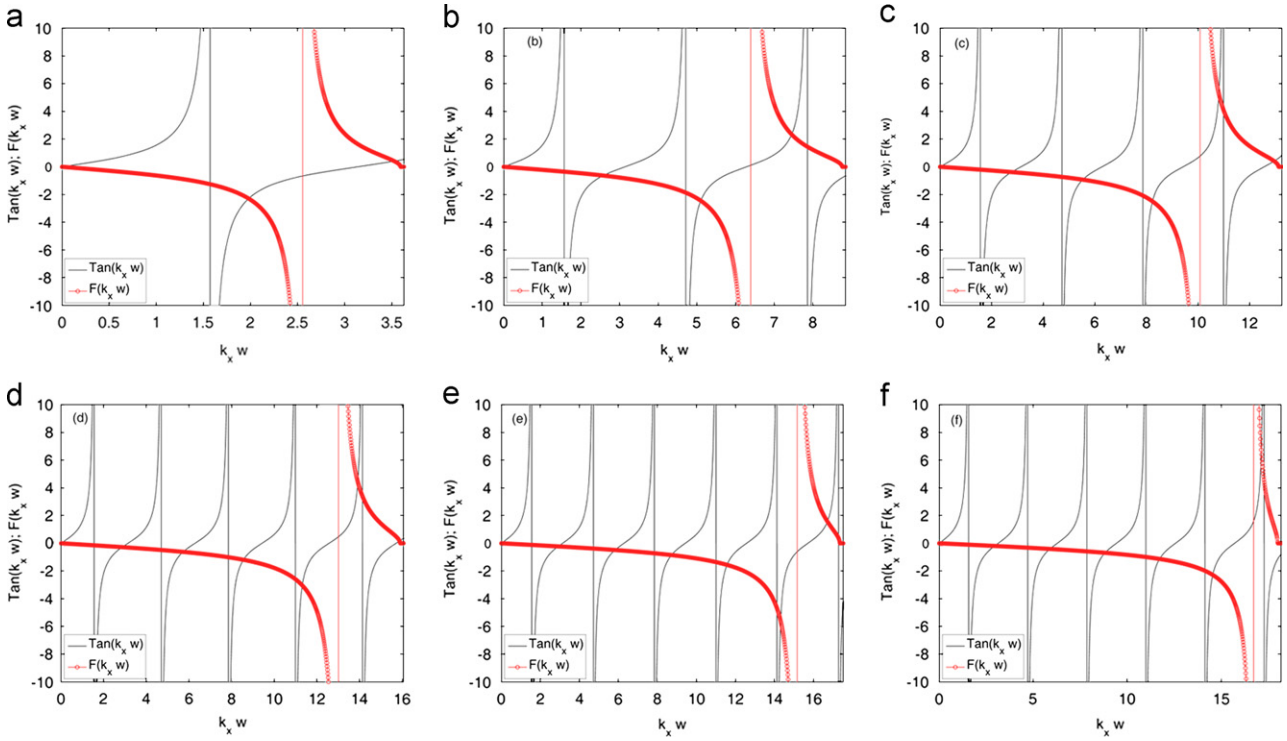

Fig. 2. Graphical determination of $k_x w$ for oscillating guided modes, with the intersections denoting the existence of guided modes. The solid and the dashed curves denote $tan(k_x w)$ and $F(k_x w)$, respectively, where physical parameters are chosen to be: $V=40$ meV, $w=200$ nm, $\zeta_2=1$ and $E=60$ meV, (a) $\zeta_1=0.34$, (b) $\zeta_1=0.38$, (c) $\zeta_1=0.48$, (d) $\zeta_1=0.68$, (e) $\zeta_1=1.08$, and (f) $\zeta_1=2.08$.

the first-order mode, second-order mode and higher order mode have similar cutoff velocities. In previous works [24,25], it is shown the magnitude of potential in barrier can be use to control the guided modes. However, in this present work, a velocity barrier can also be well applied to control the guiding of the electron wave in graphene waveguide, owing to the cutoff velocity of each mode.

3.2. Wavefunctions of guided modes and localized current density

In order to demonstrate how a velocity barrier controls the charge carriers conveyed along the channel of graphene waveguide, the wavefunctions of guided modes and the localized current density are presented in this section. As an example, the guided modes with the highest-order in Fig. 2(b)–(d) are calculated and discussed. According to Fig. 2(b)–(d), the highest orders of guided modes are second-order, fourth-order and fifth-order, respectively. The corresponding wave functions Φ_A and $-i\Phi_B$ of the highest-order guided modes, as functions of the distance of the graphene waveguide are shown in Fig. 4(a)–(c). It is clearly seen that the wavefunctions are standing waves with the number of peaks equal to the number of modes in the well region and decay exponentially in the barrier regions. In spite of the similar characteristics between the two states Φ_A and $-i\Phi_B$, a tiny shift occurs and results from the different phases between the two wave functions. Owing to the confinement of quantum well, electron mainly propagates along the y-directional channel and yields the y-directional flux. Fig. 4(d)–(f) shows the contour plots of the current densities J_y along the y coordinate for the highest-order guided modes. From Fig. 4(d)–(f), it can be seen that parts of currents can tunnel through the p–n interface and increase with the increase of the order. These tunneling currents are carried by many transverse modes, which lead to a redistribution of current at the p–n interface and the interface conductance. However, as shown in Fig. 4(d)–(f), most of currents inside the conductor are

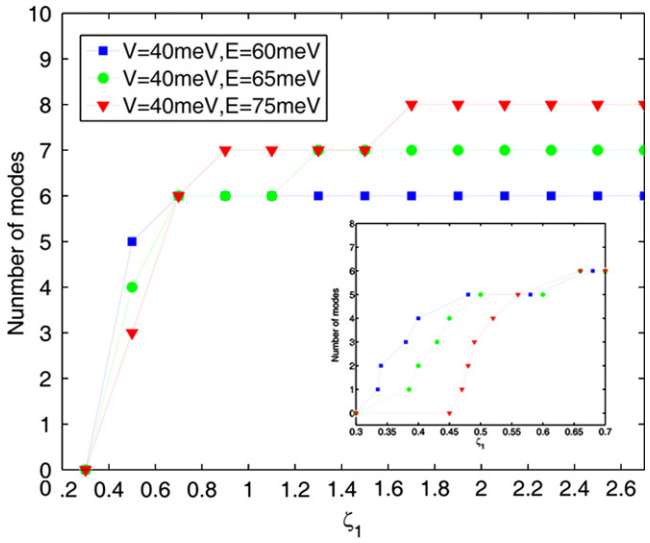

Fig. 3. The number $M(\zeta_1)$ of guided modes as a function of the velocity ζ_1 of barrier region with physical parameters $V=40$ meV, $w=200$ nm, $\zeta_2=1$, $E=60$ meV, $E=65$ meV and $E=75$ meV. The inset shows the number of guided modes for the velocity ζ_1 from 0.3 to 0.7.

carried by a discrete number of modes. In addition, the higher the order of the guided mode is, the more the number of the channel conveying the current is. As each conducting mode independently contributes to $2e^2/h$ conductance, the accumulated conduction is decided by all the conducting modes and can be expressed by $(2e^2/h)M(\zeta_1)$ with the number of guided modes $M(\zeta_1)$. Because the number of guided modes $M(\zeta_1)$ is quantized for velocity ζ_1, as previously shown in Fig. 3, the conductance $(2e^2/h)M(\zeta_1)$ along the channel should be quantized for velocity ζ_1. It is known that

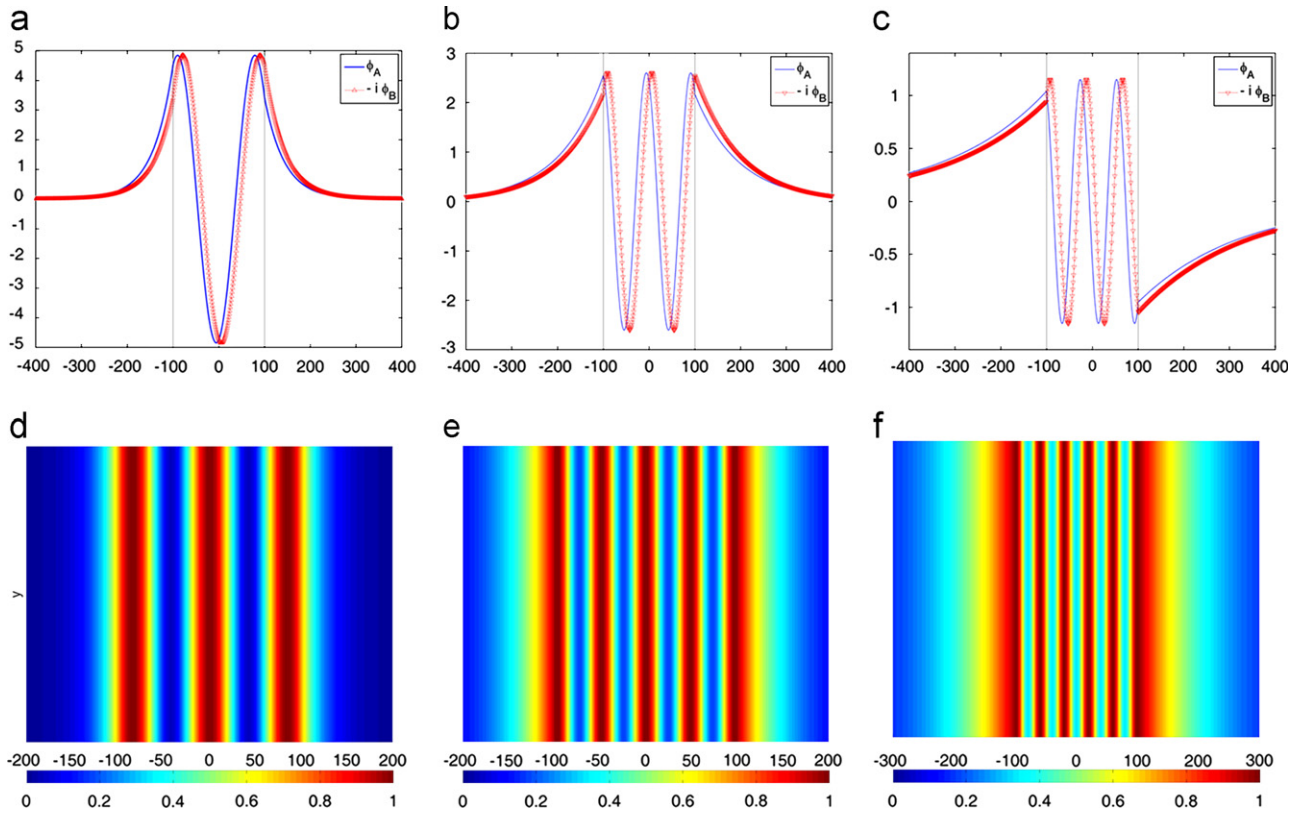

Fig. 4. Corresponding to the highest-order guided modes in Fig. 2(b)–(d), the wave function of the highest-order guided modes as a function of the distance of graphene waveguide: (a) $k_x w=7.45$, (b) $k_x w=12.95$, and (c) $k_x w=15.86$ with the corresponding probability current density: (d), (e) and (f), respectively.

conductance of graphene waveguide has a quantized feature for incident energy [15,16]. However, in the presence of a velocity barrier, the conductance of graphene waveguide can present a steplike feature for velocity.

3.3. Goos–Hänchen effect

For a graphene waveguide, the electron wave inside the channel is subject to multiple reflections at the interface of waveguide and the GH shift occurs, as shown in Fig. 1. In the case of $E > V$, the interface is created by a unipolar n–n junction, on the other hand, the interface becomes the one induced by a bipolar p–n junction with $E < V$. Fig. 5(a) and (b) present the GH shifts as functions of the incident angle at the interface with $V/E=1.5$ and 0.5, respectively, at some specific velocities. It is clearly shown that the velocity has a strong influence on the GH shift in the two cases. As shown in Fig. 5(a), all the GH shifts at the n–n interface are positive and the angle range of the GH effect is enlarged with increasing the velocity ζ_1. In Fig. 5(b), it is seen that an angle occurs with $\theta^*=\arcsin[(\sin\theta_c)^{1/2}]$ determining the sign change of GH shift at the p–n interface with $V/E=0.5$ [15]. Furthermore, it is obviously shown that the angle θ^* increases with increasing the velocity ζ_1 of barrier regions.

Fig. 5(c) further presents the GH shift as a function the velocity ζ_1 with fixed $V/E=0.1$ at some specific incident angles. It is indicated that the GH shift decreases with increasing the velocity ratio ζ_1. Considering the incident angles as a constant with $\theta=20^\circ$, the GH shift as a function of the velocity ζ_1 at the n–n or p–n junctions is shown in Fig. 5(d). It can be seen that the GH shift at the n–n interface obviously decreases and the magnitude of the negative GH shift at the p–n interface decreases and the negative GH shift can become positive with increasing the velocity.

All results indicate that the GH shift can be controlled by changing the magnitude of the velocity barrier. It is known that the Goos–Hänchen shift at the n–n or p–n interfaces of graphene waveguide can obviously change the conduction by lifting the degeneracy of spin and valley [15,17]. In addition, previous works have shown that the width and magnitude of quantum well can be adjusted to control the conduction of graphene waveguide along the channel [15]. However, in this present work, it is indicated that a velocity barrier can be used to manipulate the conduction of graphene waveguide. Finally, it should also be mentioned that the electronic tunneling through a standard graphene double barrier has been investigated and used to assess the lateral shifts of reflected and transmitted beams [19,38]. Similarly, one can also use the reflection and transmission through a double velocity barrier to present the lateral shifts of reflected and transmitted beams.

4. Conclusion

In this paper, we investigate the influence of velocity on the guided modes, localized current density inside the channel and the Goos–Hänchen shift at the n–n or p–n interfaces of graphene waveguide in the presence of a velocity barrier. It is found that a cutoff velocity determining the appearance of each guided mode occurs. Furthermore, the number of guided modes and the localized current density inside the channel can be controlled by the velocity of the barrier regions. The conductance of graphene waveguide along the channel presents a quantized feature for velocity. At last, it is also shown that the Goos–Hänchen shift at the interfaces of graphene waveguide can be well controlled by the velocity barrier. The velocity-controlled guided mode and Goos–Hänchen shift in graphene waveguide

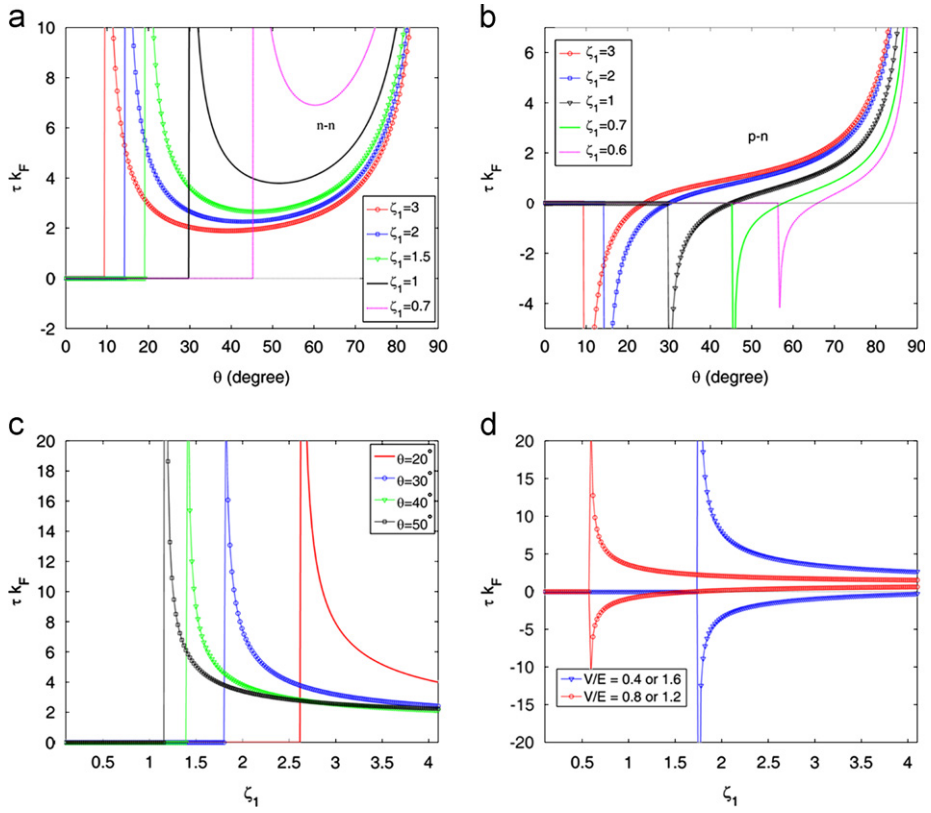

Fig. 5. Dependence on the angle of incidence θ of the GH shift τk_F, calculated from Eq. (13) for: (a) $\zeta_1=3$, 2, 1.5, 1 and 0.7 with $V/E=1.5$, (b) $\zeta_1=3$, 2, 1, 0.7 and 0.6 with $V/E=0.5$. Dependence on the velocity ζ_1 of the GH shift τk_F, calculated from Eq. (13) for: (c) $\theta=20^\circ$, 30°, 40° and 50° with $V/E=0.1$, (d) $V/E=0.4$ or 1.6, and 0.8 or 1.2 with $\theta=20^\circ$.

also demonstrate electronic analogies of optical behaviors in low-dimensional electron gas system [39,40].

Acknowledgment

This work was supported by the NSFC (Nos. 10902128, 10732100 and 11072271).

References

[1] K.S. Novoselov, A.K. Geim, S.V. Morozov, D. Jiang, Y. Zhang, S.V. Dubonos, I.V. Grigorieva, A.A. Firsov, Science 306 (2004) 666.
[2] K.S. Novoselov, A.K. Geim, S.V. Morozov, D. Jiang, M.I. Katsnelson, I.V. Grigorieva, S.V. Dubonos, A.A. Firsov, Nature 438 (2005) 197;
Y. Zhang, Y.W. Tan, H.L. Stromer, P. Kim, Nature 438 (2005) 201.
[3] V.M. Apalkov, T. Chakraborty, Physical Review Letters 97 (2006) 126801;
X. Du, I. Skachko, F. Duerr, A. Luican, E.Y. Andrei, Nature 462 (2009) 192.
[4] A.K. Geim, K.S. Novoselov, Nature Materials 6 (2007) 183.
[5] C.W.J. Beenakker, Reviews of Modern Physics 80 (2008) 1337.
[6] A.H. Castro Neto, F. Guinea, N.M.R. Peres, K.S. Novoselov, A.K. Geim, Reviews of Modern Physics 81 (2009) 109.
[7] B. Özyilmaz, P. Jarillo-Herrero, D. Efetov, D.A. Abanin, L.S. Levitov, P. Kim, Physical Review Letters 99 (2007) 166804;
B. Huard, J.A. Sulpizio, N. Stander, K. Todd, B. Yang, D. Goldhaber-Gordon, Physical Review Letters 98 (2007) 236803;
J.R. Williams, L. DiCarlo, C.M. Marcus, Science 317 (2007) 638;
T. Ihn, J. Güttinger, F. Molitor, S. Schnez, E. Schurtenberger, A. Jacobsen, S. Hellmüller, T. Frey, S. Dröscher, C. Stampfer, K. Ensslin, Materials Today 13 (2010) 44.
[8] M.I. Katsnelson, K.S. Novoselov, A.K. Geim, Nature Physics 2 (2006) 620;
A.F. Young, P. Kim, Nature Physics 5 (2009) 222.
[9] V.V. Cheianov, V. Fal'ko, B.L. Altshuler, Science 315 (2007) 1252.
[10] C.-H. Park, Y.-W. Son, L. Yang, M.L. Cohen, S.G. Louie, Nano Letters 8 (2008) 2920.
[11] M. Barbier, F.M. Peeters, P. Vasilopoulos, J. Milton Pereira Jr., Physical Review B 77 (2008) 115446;
J. Sun, H.A. Fertig, L. Brey, Physical Review Letters 105 (2010) 156801.
[12] C.-H. Park, L. Yang, Y.-W. Son, M.L. Cohen, S.G. Louie, Nature Physics 4 (2008) 213;
L.G. Wang, S.Y. Zhu, Physical Review B 81 (2010) 205444.
[13] M. Barbier, P. Vasilopoulos, F.M. Peeters, Physical Review B 81 (2010) 075438.
[14] F. Goos, H. Hänchen, Annals of Physics 436 (1947) 333;
440 (1949) 251.
[15] C.W.J. Beenakker, R.A. Sepkhanov, A.R. Akhmerov, J. Tworzydło, Physical Review Letters 102 (2009) 146804.
[16] Z. Wu, F. Zhai, F.M. Peeters, H.Q. Xu, K. Chang, Physical Review Letters 106 (2011) 176802.
[17] M. Sharma, S. Ghosh, Journal of Physics: Condensed Matter 23 (2011) 055501.
[18] X. Chen, J.-W. Tao, Y. Ban, European Physical Journal B 79 (2011) 203.
[19] Y. Song, H.-C. Wu, Y. Guo, Applied Physics Letters 100 (2012) 253116.
[20] W. Häusler, A. De Martino, T.K. Ghosh, R. Egger, Physical Review B 78 (2008) 165402;
R.R. Hartmann, N.J. Robinson, M.E. Portnoi, Physical Review B 81 (2010) 245431;
N. Myoung, G. Ihm, S.J. Lee, Physical Review B 83 (2011) 113407;
W. Huang, Y. He, Y. Yang, C. Li, Journal of Applied Physics 111 (2012) 053712.
[21] A. De Martino, L. Dell' Anna, R. Egger, Physical Review Letters 98 (2007) 066802;
M. Ramezani Masir, P. Vasilopoulos, F.M. Peeters, Applied Physics Letters 93 (2008) 242103.
[22] F. Guinea, M.I. Katsnelson, A.K. Geim, Nature Physics **6** (2010) 30.
[23] H. Li, L. Wang, Z. Lan, Y. Zheng, Physical Review B 79 (2009) 155429.
[24] J.Milton Pereira Jr., V. Mlinar, F.M. Peeters, P. Vasilopoulos, Physical Review B 74 (2006) 045424.
[25] F.-M. Zhang, Y. He, X. Chen, Applied Physics Letters 94 (2009) 212105.
[26] Z. Wu, Applied Physics Letters 98 (2011) 082117.
[27] L. Zhao, S.F. Yelin, Physical Review B 81 (2010) 115441;
Y.P. Bliokh, V. Freilikher, F. Nori, Physical Review B 81 (2010) 075410.
[28] J.R. Williams, T. Low, M.S. Lundstrom, C.M. Marcus, Nature Nanotechnology 6 (2011) 222.
[29] A. Raoux, M. Polini, R. Asgari, A.R. Hamilton, R. Fazio, A.H. MacDonald, Physical Review B 81 (2010) 073407.

[30] A. Gibertini, V. Singha, M. Pellegrini, G. Polini, A. Vignale, L.N. Pinczuk, Pfeiffer, K.W. West, Physical Review B 79 (2009) 241406.
[31] A. Concha, Z. Tešanović, Physical Review B 82 (2010) 033413.
[32] P.M. Krstajić, P. Vasilopoulos, Journal of Physics: Condensed Matter 23 (2011) 135302.
[33] G. Borghi, M. Polini, R. Asgari, A.H. MacDonald, Solid State Communications 149 (2009) 1117.
[34] J.-H. Yuan, Z. Cheng, Q.-J. Zeng, J.-P. Zhang, J.-J. Zhang, Journal of Applied Physics 110 (2011) 103706.
[35] F. de Juan, A. Cortijo, M.A.H. Vozmediano, Physical Review B 76 (2007) 165409;
N.M.R. Peres, Journal of Physics: Condensed Matter 21 (2009) 095501.
[36] A. Esmailpour, H. Meshkin, R. Asgari, Solid State Communications 152 (2012) 1896.
[37] C.-F. Li, Physical Review Letters 91 (2003) 133903.
[38] J. Milton Pereira Jr., P. Vasilopoulos, F.M. Peeters, Applied Physics Letters 90 (2007) 132122.
[39] S. Datta, Electronic Transport in Mesoscopic Systems, Cambridge University Press, New York, 1995, pp. 276–290.
[40] D. Dragoman, M. Dragoman, Quantum-Classical Analogies, Springer, Berlin, 2004.